Numerical study of turbulent in-cylinder flow during motoring utilizing a general curvilinear coordinate system

C. P. Chiu and T. S. Wu
Department of Mechanical Engineering, National Cheng Kung University, Tainan, Taiwan, Republic of China

A finite-volume numerical calculation method is presented to predict the flow field at unsteady, turbulent levels in a motoring reciprocating engine. An algebraic grid generation technique is used to map the complex fluid domain, on which the cylinder head is a deformed boundary, onto a rectangle for every time step. Hence the metric of the coordinate transformation can be determined by direct analytic differentiation. The model gives a good account of the axial, radial, and swirl velocity components and engine turbulence by means of a two-equation model of turbulence and wall functions. Effects of the shapes of both cylinder head and grid distribution on in-cylinder air motion are investigated.

Keywords: algebraic grid generation technique; deformed boundary; in-cylinder air motion; unsteady turbulent flow

Introduction

Body-fitted coordinate systems have been utilized in conjunction with finite-difference techniques to solve steady-flow problems with an irregularly physical domain.[1-3] The physical domain, in which the boundaries are always irregularly shaped, is generally mapped onto a rectangular computational domain. Mapping of the domain is achieved by what are known as grid generation techniques, which may be roughly grouped into two categories: differential equation techniques and algebraic grid generation techniques.[4] The methods that generate the grid by solving a system of partial differential equations, developed largely by Thompson *et al.*,[5] are called differential equation techniques. Algebraic grid generation techniques do not require the solution of partial differential equations; rather, an algebraic nonorthogonal coordinate transformation is used. Consequently, algebraic grid generation techniques are computationally much more efficient than differential equation methods. This difference is especially true for unsteady problems, in which grid points are moving in the physical domain.

Algebraic grid generation techniques have been applied to viscous laminar flow under steady state.[6,7] The methodology was developed for nonorthogonal curvilinear systems. A fully staggered grid system is used to calculate the velocity and pressure fields in order to avoid spurious pressure oscillations. Hence no explicit description of the pressure boundary condition is needed. A rectangular computational domain is obtained by using Moretti's transformation, making possible avoidance of the task of solving a system of partial differential equations. The numerical results are in excellent agreement with the available analytical solutions.

That in-cylinder air motion greatly influences the combustion process is generally accepted. Many parameters affect in-cylinder air motion, such as initial swirl ratio, engine speed, wall heat transfer, chemical reactions, turbulent transport, combustion chamber geometries, etc.[8,9] Several studies on the effects of combustion chamber geometries have shown that geometry greatly influences the flow pattern.[8-11] In order to economically design and improve the performance of combustion systems in reciprocating engines, therefore, development of useful computer programs to simulate internal engine flow is important.

Differential grid generation techniques have been applied to solve in-cylinder air motion with a cup in the piston head.[8,12] The grid points inside the cup are stationary, i.e., do not vary with time as the piston moves. Itoh *et al.*[13] utilized a method based on the algorithm of CONCHAS-SPRAY to examine in-cylinder air motion in a "flat hemisphere" combustion chamber. A nonstaggered grid system was adopted.

In our previous study,[14] we applied algebraic grid generation techniques to simulate in-cylinder air motion involving a physical domain that varies over time under laminar conditions. Therefore a fixed computational region is mapped for every time step. Air flow in real reciprocating engines is very complicated and behaves as turbulent motion.[9] In the present study we extend the discussion further to unsteady, axisymmetric turbulent air motion. Hence the methodology of our previous study proved to be very useful.

Transformation of grid systems

Figure 1 shows the physical and computational domains for calculation of the in-cylinder flow fields. In the physical domain, only half the cylinder is considered because of symmetry. The head of the engine's combustion chamber is a deformed hemisphere and the piston head is flat.

For two-dimensional (2-D) spatial domains varying with time, three dependent variables (ξ, η, and τ) are used to transform the governing equation from the physical domain to the computational domain (Figure 1). The terms (x, r, t) represent the physical domain and (ξ, η, τ) represent the computational domain. Here, f_1, f_2, etc., are boundaries in the physical domain and are functions defined only at these boundaries. Therefore, based on Moretti's transformation,[15] ξ

Address reprint requests to Professor Chiu at the Department of Mechanical Engineering, National Cheng Kung University, Tainan, Taiwan, Republic of China.

Received 1 November 1989; accepted 15 May 1990

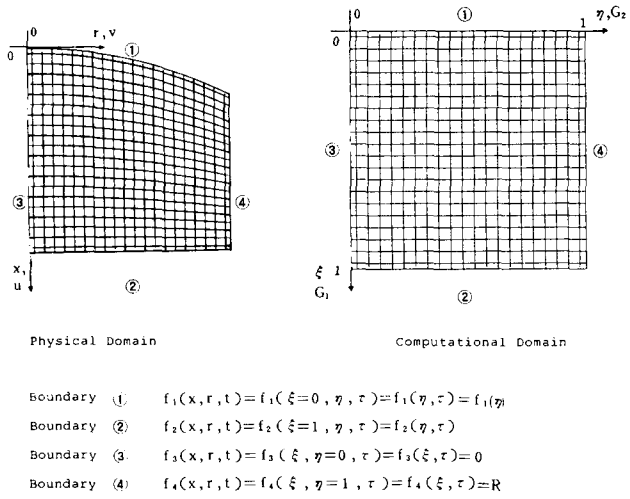

Figure 1 Schematic diagram of the physical and computational domains

and η are defined as follows:

$$\xi=\frac{x-f_1(x,r,t)}{f_2(x,r,t)-f_1(x,r,t)} \quad \text{and} \quad \eta=\frac{r-f_3(x,r,t)}{f_4(x,r,t)-f_3(x,r,t)} \tag{1}$$

so

$$\xi=\xi(x,r,t) \quad \text{and} \quad \eta=\eta(x,r,t) \tag{2}$$

Conversely,

$$x=x(\xi,\eta,\tau) \quad \text{and} \quad r=r(\xi,\eta,\tau) \tag{3}$$

The relationship between t and τ is taken to be

$$t=\tau \tag{4}$$

i.e., there is no stretching in time.

Explicit functional relationships between the physical and computational domains are based on this transformation. The grid lines are specified in equally spaced increments in the ξ and η directions, where the ranges of ξ and η are

$$0\le\xi\le1 \tag{5}$$

$$0\le\eta\le1 \tag{6}$$

Then, Equation 1 becomes

$$x=f_2(\eta,\tau)\xi+f_1(\eta,\tau)(1-\xi) \tag{7}$$

$$r=f_4(\xi,\tau)\eta+f_3(\xi,\tau)(1-\eta) \tag{8}$$

Introducing the new dependent variables, ξ and η, and applying the chain rule for partial derivatives transforms the original partial differential equation from the physical domain (x, r, t) to the computational domain (ξ, η, τ):

$$\begin{pmatrix}\dfrac{\partial\phi}{\partial t}\\ \dfrac{\partial\phi}{\partial x}\\ \dfrac{\partial\phi}{\partial r}\end{pmatrix}=\begin{pmatrix}\xi_t & \eta_t\\ \xi_x & \eta_x\\ \xi_r & \eta_r\end{pmatrix}\begin{pmatrix}\dfrac{\partial\phi}{\partial\xi}\\ \dfrac{\partial\phi}{\partial\eta}\end{pmatrix} \tag{9}$$

where

$$\begin{pmatrix}\xi_t & \eta_t\\ \xi_x & \eta_x\\ \xi_r & \eta_r\end{pmatrix}$$

is called the metrics of the transformation.

The metrics of the transformation can be analytically calculated when known functions are used in the boundaries.

Clearly, the relationship between the physical and computational domains need to be determined. This relationship establishes the metrics of the transformation. These quantities can also be obtained from the expressions:

$$\xi_x=\frac{r_\eta}{\mathrm{J}} \tag{10}$$

$$\xi_r=\frac{-x_\eta}{\mathrm{J}} \tag{11}$$

$$\eta_x=\frac{-r_\xi}{\mathrm{J}} \tag{12}$$

$$\eta_r=\frac{x_\xi}{\mathrm{J}} \tag{13}$$

Notation

f_1, f_2, f_3, f_4	Functions of the boundary wall curve
G_1, G_2	Contravariant velocity
J	Jacobian metric
k	Turbulent kinetic energy
L	Turbulent length
N	Engine speed
P	Pressure
q_1, q_2, q_3	Geometric relations between coordinate systems
R	Radius of cylinder
s	Source term in governing equations for the physical plane
S	Source term in governing equations for the transformed plane
t, τ	Time
u, v, w	Velocity components along x, r, and θ axes
U_{pis}	Velocity of moving piston
x, r	Cylindrical coordinates

Greek symbols

ρ	Density
ϕ	General dependent variable
Ω	Swirl ratio
Γ	Diffusion coefficient
μ	Viscosity
ξ, η, τ	Transformed coordinate
δ_1, δ_2	$\delta_1=f_2-f_1$; $\delta_2=f_4-f_3$
$\mathcal{V}$	Volume of the control volume
ε	Rate of dissipation of turbulent kinetic energy

Subscripts

E, W, N, S	Four nodes adjacent to P
e, w, n, s	Four surfaces of control volume centered at P
P	Nodal point to be solved for in difference equation
x, r, t	Partial derivative with respect to x, r, and t
ξ, η, τ	Partial derivative with respect to ξ, η, and τ

Superscripts

0	Value at the previous time step

where J is called Jacobian matrix, or

$$J = x_\xi r_\eta - r_\xi x_\eta = \frac{1}{\xi_x \eta_r - \xi_r \eta_x} \tag{14}$$

For the wall of the cylinder, which is straight and is independent of time, both f_3 and f_4 are constant. The cylinder head is stationary, so f_1 is also independent of time. Let

$$\delta_1(\eta, \tau) = f_2(\eta, \tau) - f_1(\eta, \tau) = f_2(\eta, \tau) - f_1(\eta) \tag{15}$$

$$\delta_2(\xi, \tau) = f_4(\xi, \tau) - f_3(\xi, \tau) = \text{Constant} = R \tag{16}$$

where R is the radius of the cylinder, δ_1 is the distance between the moving boundary (the piston head) and the fixed end (the cylinder head). As δ_1 is a function of time and δ_2 are constants,

$$\xi_t = -\frac{\xi}{\delta_1}\frac{d\delta_1}{dt} \quad \text{and} \quad \eta_t = 0 \tag{17}$$

Note that $U_{\text{pis}} = d\delta_1/dt$ and that δ_1 is function of radius and time.

The main advantages of using algebraic grid generation are that they are direct and that the metrics of the transformation can be computed analytically.

The grids inside the combustion chamber contract or expand according to the motion of the piston, as shown (for example) in Figure 2 for the flat hemisphere case. A transformation of coordinates is introduced to transfer the moving boundary value problem into a fixed boundary value problem. The piston is always located at $\xi = 1$ in the transformed domain. Therefore a fixed computational region is obtained.

The generating of grid points is demonstrated by means of a 2-D time-varying spatial domain. However, the technique presented here can readily be extended to three-dimensional (3-D) spatial domains that vary with time.

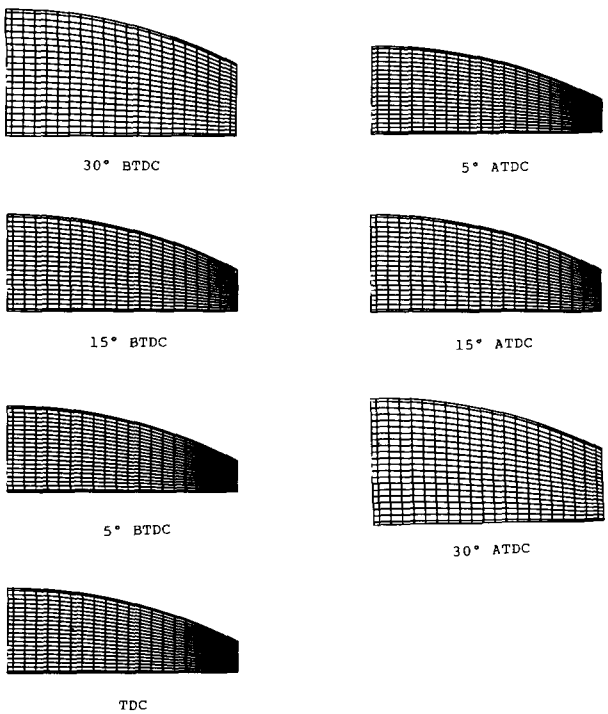

Figure 2 Grid points during compression and expansion strokes in flat hemisphere combustion chamber (22 × 22 grid points)

Governing equations and mathematical model

Unsteady, incompressible, nonreacting, turbulent in-cylinder flow can be described by the Reynolds-averaged equations and k–ε turbulence model.[16,17] The time-dependent governing equations can be written in axisymmetric cylindrical (x, r, t) coordinates:

$$\frac{\partial(\rho\phi)}{\partial t} + \frac{1}{r}\left[\frac{\partial}{\partial x}(\rho u r \phi) + \frac{\partial}{\partial r}(\rho v r \phi)\right] = \frac{1}{r}\left[\frac{\partial}{\partial x}\left(t\Gamma\frac{\partial\phi}{\partial x}\right) + \frac{\partial}{\partial r}\left(r\Gamma\frac{\partial\phi}{\partial r}\right)\right] + s(x, r) \tag{18}$$

where ρ, Γ, and s denote the density, diffusion coefficient, and source terms, respectively. Also, ϕ represents one of the following entities: 1, u, v, w, k, or ε, in which the dependent variables are axial velocity u, radial velocity v, swirl velocity w, and turbulent kinetic energy k and its dissipation rate ε. The definitions of ϕ, Γ, and s are shown in Tables 1 and 2.[17] The pressure gradient terms are combined into the source terms.

After some rearrangement, Equation 18 can be rewritten in strong conservation-law form as

$$\frac{1}{\delta_1}\frac{\partial(\rho\delta_1\phi)}{\partial\tau} + \frac{1}{r}\left[\frac{\partial}{\partial\xi}(\rho r G_1 \phi) + \frac{\partial}{\partial\eta}(\rho r G_2 \phi)\right] = \frac{1}{r}\left\{\frac{\partial}{\partial\xi}\left[\Gamma r\left(q_1\frac{\partial\phi}{\partial\xi} + q_2\frac{\partial\phi}{\partial\eta}\right)\right] + \frac{\partial}{\partial\eta}\left[\Gamma r\left(q_2\frac{\partial\phi}{\partial\xi} + q_3\frac{\partial\phi}{\partial\eta}\right)\right]\right\} + S(\xi, \eta) \tag{19}$$

Table 1 Definition of ϕ, Γ, and s

ϕ	Γ	s
1	0	0
u	μ_{eff}	$-\frac{\partial p}{\partial x} + \frac{\partial}{\partial x}\left(\mu_{\text{eff}}\frac{\partial u}{\partial x}\right) + \frac{1}{r}\frac{\partial}{\partial r}\left(\mu_{\text{eff}} r\frac{\partial v}{\partial x}\right) - \frac{2}{3}\frac{\partial}{\partial x}[\mu_{\text{eff}}(\nabla\cdot\vec{u}) + \rho k]$
v	μ_{eff}	$-\frac{\partial p}{\partial r} + \frac{\partial}{\partial x}\left(\mu_{\text{eff}}\frac{\partial u}{\partial r}\right) + \frac{1}{r}\frac{\partial}{\partial r}\left(\mu_{\text{eff}} r\frac{\partial v}{\partial r}\right) - 2\mu_{\text{eff}}\frac{v}{r^2} + \frac{\rho w^2}{r} - \frac{2}{3}\frac{\partial}{\partial r}[\mu_{\text{eff}}(\nabla\cdot\vec{u}) + \rho k]$
w	μ_{eff}	$-\left[\frac{\rho v}{r} + \frac{1}{r^2}\frac{\partial}{\partial r}(r\mu_{\text{eff}})\right]w$
k	$\frac{\mu_{\text{eff}}}{\sigma_k}$	$G_k - \rho\varepsilon$
ε	$\frac{\mu_{\text{eff}}}{\sigma_\varepsilon}$	$C_1 G_k \varepsilon/k - C_2\rho\varepsilon^2/k + (1 - C_3)\rho\varepsilon(\nabla\cdot\vec{u})$

$$G_k = \mu_{\text{eff}}\left\{2\left[\left(\frac{\partial u}{\partial x}\right)^2 + \left(\frac{\partial v}{\partial r}\right)^2 + \left(\frac{v}{r}\right)^2\right] + \left(\frac{\partial v}{\partial x} + \frac{\partial u}{\partial r}\right)^2 + \left(\frac{\partial w}{\partial x}\right)^2 + \left[r\frac{\partial}{\partial r}\left(\frac{w}{r}\right)\right]^2\right\} - \frac{2}{3}(\nabla\cdot\vec{u})\{\mu_{\text{eff}}(\nabla\cdot\vec{u}) + \rho k\}$$

$$\mu_{\text{eff}} = \frac{C_d\rho k^2}{\varepsilon} + \mu_{\text{lam}}$$

Table 2 Empirical coefficients used for the k–ε model

$C_1 = 1.44$	$C_2 = 1.0$	$C_3 = 1.373$
$\sigma_k = 1.0$	$\sigma_\varepsilon = 1.3$	$C_d = 0.09$

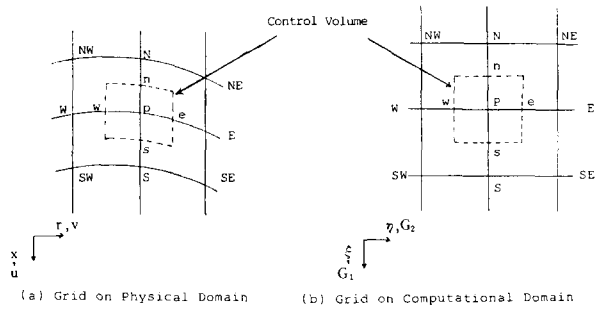

Figure 3 Types of grid systems in the physical and computational domains

where

$$G_1 = u\xi_x + v\xi_r + \xi_t \tag{20}$$

$$G_2 = u\eta_x + v\eta_r \tag{21}$$

$$q_1 = \xi_x^2 + \xi_r^2 \tag{22}$$

$$q_2 = \xi_x\eta_x + \xi_r\eta_r \tag{23}$$

$$q_3 = \eta_x^2 + \eta_r^2 \tag{24}$$

where G_1 and G_2 are the contravariant velocities written without metric normalization.

Figure 3 shows the finite-volume grid system in the physical and computational domains. A fully staggered grid system is adopted, with the swirl velocity w and scalar variables P, ρ, k, ε, etc., are located at the grid nodes P, E, etc. The velocity quantities are located at the midpoints of the grid joints: u at the e–w faces of the control volume and v at the n–s faces.

The control volume of integration $d\mathbb{V}$ is

$$d\mathbb{V} = r\,dx\,dr = r\delta_1\delta_2\,d\xi\,d\eta = rJ\,d\xi\,d\eta \tag{25}$$

where $J = \delta_1\delta_2$.

Integration of Equation 19 over the control volume $d\mathbb{V}$ gives

$$\int \left\{ \frac{1}{\delta_1}\frac{\partial(\rho\delta_1\phi)}{\partial\tau} + \frac{1}{r}\left[\frac{\partial}{\partial\xi}(\rho r G_1\phi) + \frac{\partial}{\partial\eta}(\rho r G_2\phi)\right] - \frac{1}{r}\frac{\partial}{\partial\xi}\left[\Gamma r\left(q_1\frac{\partial\phi}{\partial\xi} + q_2\frac{\partial\phi}{\partial\eta}\right)\right] - \frac{1}{r}\frac{\partial}{\partial\eta}\left[\Gamma r\left(q_2\frac{\partial\phi}{\partial\xi} + q_3\frac{\partial\phi}{\partial\eta}\right)\right]\right\} d\mathbb{V} = \int (S_c + S_p\phi_p)\,d\mathbb{V} \tag{26}$$

where the source term has been made linear in the usual manner, and—for the unsteady term—S_p and ϕ_p are assumed to prevail over the entire control volume. Evaluating Equation 26 requires use of a central difference approach to approximate the diffusion term. When the values on the control volume faces are unknown, interpolation from the nodal values is required.

The continuity equation can also be written in (x, r, t) coordinates as

$$\frac{\partial\rho}{\partial t} + \frac{1}{r}\left[\frac{\partial(\rho u r)}{\partial x} + \frac{\partial(\rho v r)}{\partial r}\right] = 0 \tag{27}$$

and transformed to (ξ, η, τ) coordinates as:

$$\frac{1}{\delta_1}\frac{\partial(\rho\delta_1)}{\partial t} + \frac{1}{r}\left[\frac{\partial}{\partial\xi}(\rho r G_1) + \frac{\partial}{\partial\eta}(\rho r G_2)\right] = 0 \tag{28}$$

Integrating the continuity equation over each control volume $d\mathbb{V}$ yields the integral form:

$$\int \left\{ \frac{1}{\delta}\frac{\partial(\rho\delta_1)}{\partial t} + \frac{1}{r}\left[\frac{\partial}{\partial\xi}(\rho r G_1) + \frac{\partial}{\partial\eta}(\rho r G_2)\right]\right\} d\mathbb{V} = 0 \tag{29}$$

The molecular viscosity and density would be spatially uniform but vary temporarily at every time step for the assumption of quasi-compressible and quasi-steady states. The density is updated only from the volume of the cylinder; for example,

$$\rho = \rho^0 \frac{\mathbb{V}^0}{\mathbb{V}} \tag{30}$$

where ρ^0 and $\mathbb{V}^0$ refer to the values at previous time t. The calculations are performed for turbulent swirling flow and without heat transfer between fluid and wall.

The standard k–ε two-equation model was utilized as the turbulence model, which has an additional term in the ε equation to express the compression-dilation effect. This modification results from Morel's assessment.[16]

In order to economize on grid nodes in the region of the flow field conditions adjacent to the solid wall often are matched to some assumed boundary-layer profiles of velocity. The law-of-the-wall (wall functions) is used to provide wall boundary conditions.[18,19]

The algorithm used in the calculation is the SIMPLE algorithm, developed by S. V. Patankar.[20] After some modification, the SIMPLE algorithm and a power-law procedure were extended to the present curvilinear coordinate system, as discussed in ref. 14. The modified procedures were used successfully for unsteady laminar flow calculations.

Boundary conditions

No-slip boundary conditions are applied for velocities at all walls. At the piston head, the axial velocity u is assumed to equal the moving velocity of the piston. The normal component of the gradient of turbulent kinetic energy is set equal to zero near a solid wall, whereas the rate of dissipation of turbulent kinetic energy is calculated by the wall function.[18]

Initial conditions

The air is taken to have the solid-body rotation profiles $w(r) = 2\pi N\Omega r$, where N is the engine speed and Ω (called the swirl ratio) is defined as the ratio of swirling speed (rpm) of the gas to engine speed. The radial velocity v is assumed to be zero. The axial velocity u is assumed to vary linearly from cylinder head (zero velocity) to piston head (moving boundary velocity). Turbulence is taken to be uniform throughout the cylinder. The initial values of turbulent kinetic energy are $k = 0.012\bar{U}^2$, where $\bar{U}$ is the mean velocity. In an engine, the length L of turbulence is on the order of 0.1 times the cylinder bore D. The initial dissipation rate is calculated from $\varepsilon = C_d K^{3/2}/0.1D$.[16,17]

The engine used for computation is a four-stroke engine with a curved cylinder head. The main specifications of the engine are illustrated in Table 3.

At the start of the calculation, the proper initial operating conditions, as suggested by Itoh,[13] are specified. The swirl ratios for the initial values are 2.15 at a crank angle of 130° BTDC (before top dead center) at an engine speed of 700 rpm.

Table 3 Engine parameters

Bore × stroke	76 mm × 78 mm
Displacement volume	352.8 cc
Compression ratio	9:1
Engine speed	700 rpm
Piston head geometry	Pancake

Results and discussion

Two types of combustion chamber were considered. The first has a dome in the cylinder head, and is called a "flat hemisphere." The second has no dome and is called a "flat plate." The grids inside the combustion chamber contract or expand according to the motion of the piston.

Air motion within the combustion chamber

Figure 4 shows the flow fields at different crank angles, ranging from 30° BTDC to 30° ATDC (after top dead center), in a flat hemisphere type of combustion chamber during compression and expansion strokes. The combined values of u and v are represented in vector form as shown in Figure 4a. The corresponding swirl velocity is presented in Figure 4b. At 30° BTDC, as the piston moves toward TDC, the air inside the combustion chamber is directed toward the cylinder head because of the upward motion of the piston. The piston motion transfers air from the periphery to the cylinder axis, inducing a flow called "squish flow." Air transferred from the cylinder axis to the periphery is called "reversed squish." At TDC two vortices exist inside the combustion chamber, which are opposite in direction of rotation. The stronger counterclockwise vortex is induced from squish flow. The weaker clockwise vortex, found near the cylinder wall, is induced by interaction between the squish and swirl flows.

At 5° ATDC, the piston is moving downward, and reversed squish flow was observed. The counterclockwise vortex has disappeared and the strength of the clockwise vortex has been reduced. After 15° ATDC, the vortex disappears because of reversed squish flow and decreasing swirl velocities.

Figure 5 presents the distributions of turbulent kinetic energy and its dissipation rate at different crank angles. It has a strong peak near the boundary of the cylinder head where the strong shear layer caused by squish flow produces turbulence.

Figure 6 shows the flow field of the flat plate type of combustion chamber during compression and expansion strokes. At TDC, the strength of the counterclockwise vortex has almost disappeared. The squish flow is weaker than for the flat hemisphere combustion chamber at this position. The clockwise vortex still exists inside the combustion chamber. Thus an increase in hemisphere depth apparently raises the strength of squish flow.

Sensitivity to grid size

A further assessment of the effect of grid point distribution on the numerical results was made. In these calculations, other grid points were tested. This grid system contains 36 grid points in the radial coordinates; i.e., more points were used to describe the curved wall. The number of grid points was changed from 22×22 to 16×36. All the boundary conditions, physical parameters, and solution procedures remain the same. Figure 7 shows the grid system and the flow fields of a flat hemisphere type of combustion chamber at different crank angles. Comparing Figures 4 and 7 shows that the calculated flow fields are very similar.

To demonstrate further the sensitivity to grid size of the computer program, comparisons were tested for mean swirl ratio and local swirl velocity. Figure 8 shows the time history of the mean swirl ratios for a different combustion chamber geometry and a different grid system. Higher mean swirl ratios are obtained from the flat hemisphere combustion chamber. This result may be due to the effect of higher strength of squish flow. The mean swirl ratios, predicted on two grid systems, are very close.

Figures 9 and 10 show the comparison of local velocity at

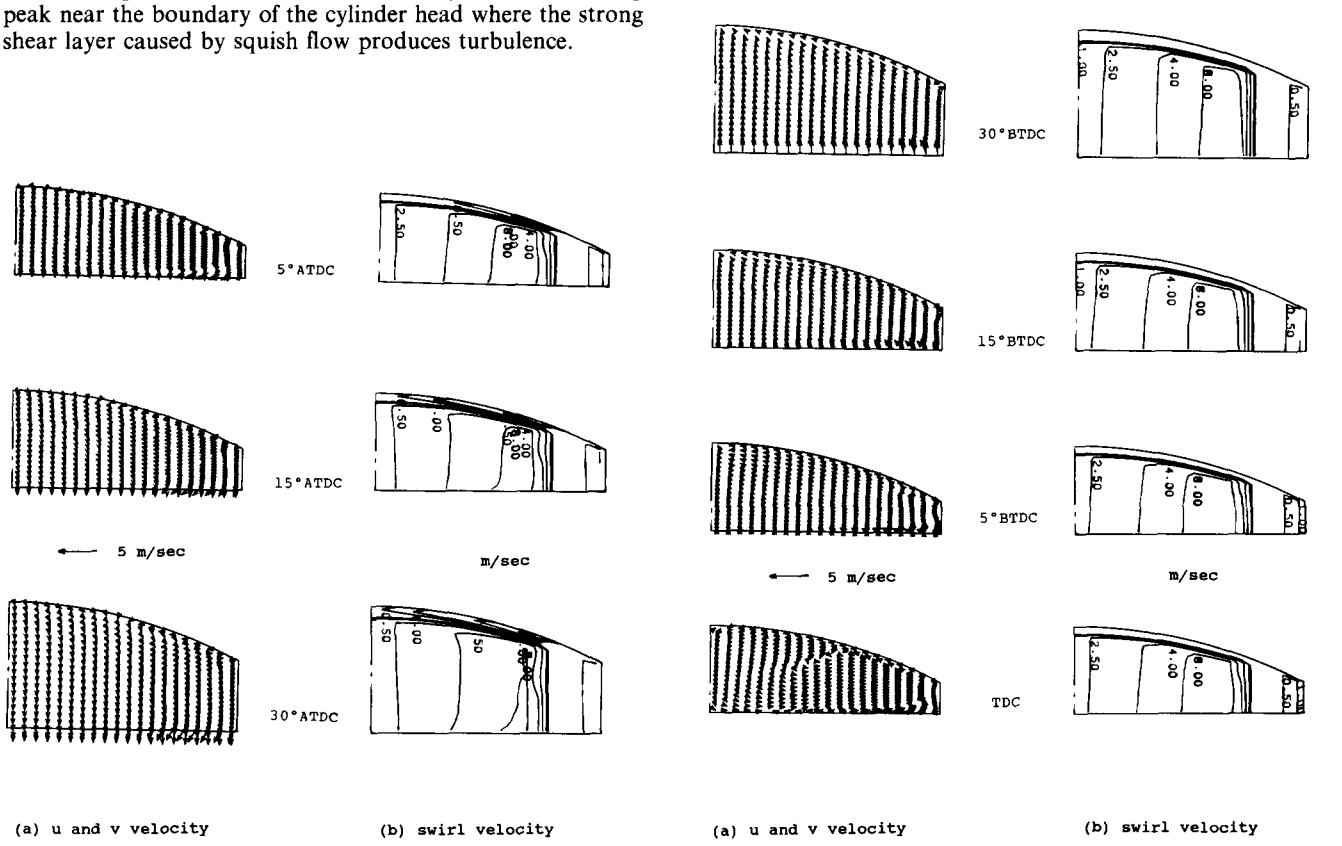

Figure 4 Flow fields at different crank angles of the flat hemisphere combustion chamber

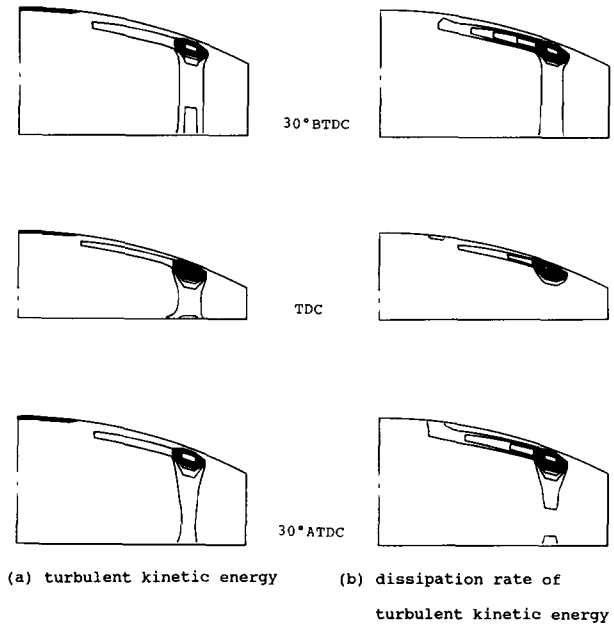

Figure 5 Distribution of turbulent kinetic energy and its dissipation rate at different crank angles of the flat hemisphere combustion chamber

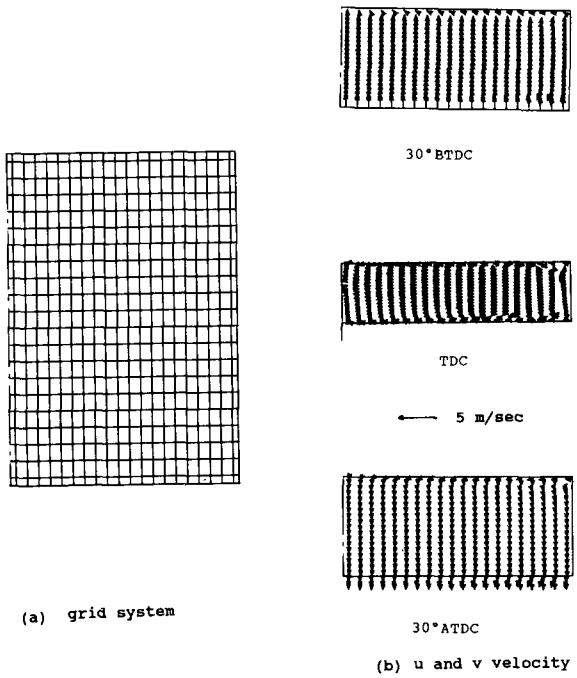

Figure 6 Grid system and flow fields at different crank angles of the flat plate combustion chamber

different points on two grid systems for the flat hemisphere type of combustion chamber. The points compared are fixed 5 mm below the top of the hemisphere. Three points were investigated: 10 mm, 15 mm, and 25 mm from the axis of the cylinder. Figure 9 shows that the calculated swirl velocities are almost the same at the two points. The overall differences

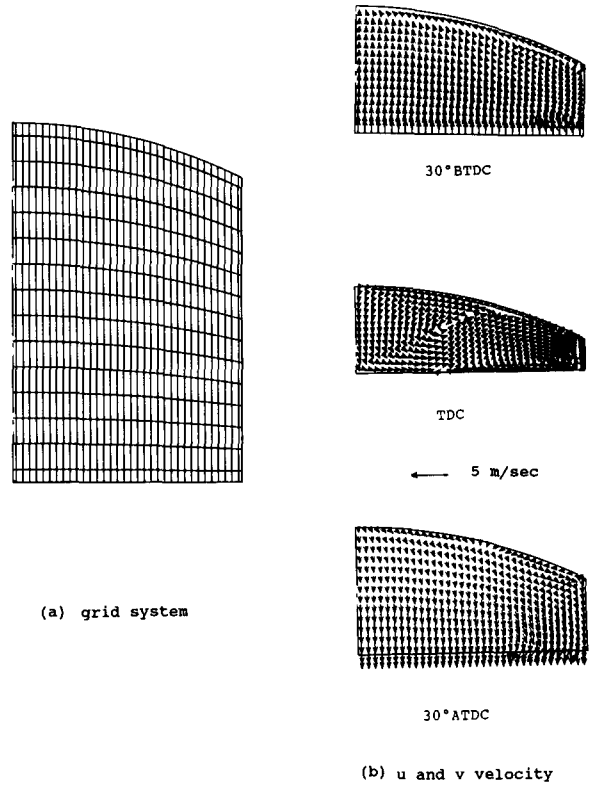

Figure 7 Grid system and flow fields at different crank angles of the flat hemisphere combustion chamber (16 × 36 grid points)

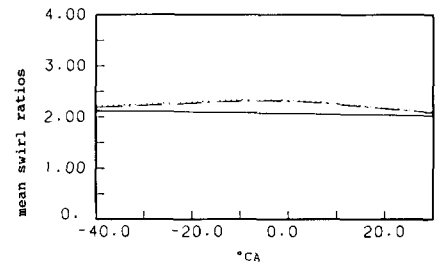

Figure 8 Time history of the mean swirl ratios: —— flat plate; – – – flat hemisphere (22 × 22 grid points); ····· flat hemisphere (16 × 36 grid points)

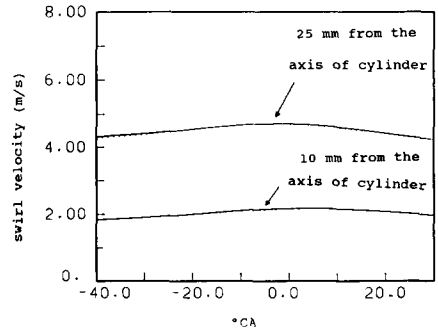

Figure 9 Comparison of local swirl velocities: —— 22 × 22 grid points; ····· 16 × 36 grid points

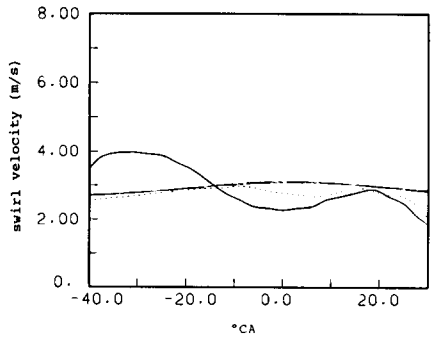

Figure 10 Comparison of calculated and experimental results: —— experimental, Itoh; ····· calculated, Itoh; ——— simulated, present study (22 × 22 grid points); — — — simulated, present study (16 × 36 grid points)

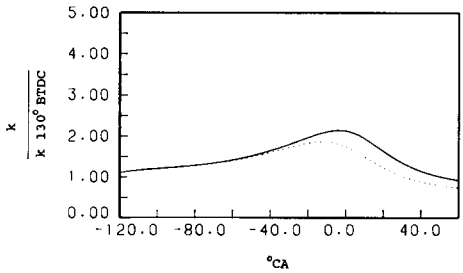

Figure 11 Time history of total turbulent kinetic energy: —— flat hemisphere and ----- flat plate combustion chambers

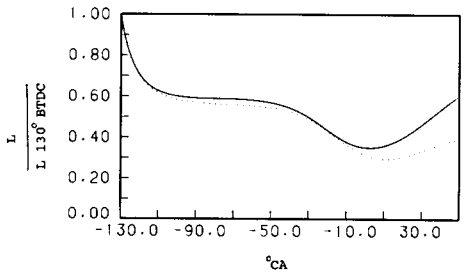

Figure 12 Time history of averaged turbulent length: —— flat hemisphere and ----- flat plate combustion chambers

between the calculated solutions on the two grid systems are quite small. Figure 10 shows the comparison with experimental data obtained by Itoh[13] for the flat hemisphere type of combustion chamber. The measuring point is located 15 mm from the axis of the cylinder and 5 mm below the top of the hemisphere. The solid line and dotted line are Itoh's experimental and calculated results. Itoh's calculations were for laminar conditions. The dashed lines are the result of simulation with the present algorithm. The data simulated in the present study almost coincide with Itoh's calculations for ATDCs of less than 25°.

Figure 11 shows the development of total turbulent kinetic energy for both cases throughout the compression–expansion cycle. The level of turbulent intensity depends on combustion chamber shape. For the flat hemisphere combustion chamber, the turbulent intensity increases steadily before TDC. Calculations for the flat hemisphere combustion chamber, with a stronger swirl air motion, predict a higher turbulent intensity than those for the flat plate combustion chamber.

Figure 12 shows the time history of averaged turbulent length for the two combustion chamber shapes. The predicted results show that the variation in length follows roughly the same trend line as the cylinder volume height. The length reaches a minimum near top dead center and increases during the following expansion stroke.

Conclusions

A time-dependent, turbulent in-cylinder flow was calculated during motoring for various combustion chamber geometries. An efficient algebraic grid generation technique was used to map the complex fluid domain onto a rectangle for every time step. The procedure for implementing this grid generation technique is described in detail. If the functions of the boundary wall curve are known, the technique can be applied easily to other engine configurations.

Other conclusions can be summarized as follows.

(1) The compression–expansion effect on in-cylinder turbulent flow field can be predicted successfully with a general curvilinear coordinate system.
(2) Calculations for the flat hemisphere type of combustion chamber predict higher levels of mean swirl ratios and total turbulent kinetic energy than those for flat plate combustion chamber.
(3) The overall differences between the calculated solutions on the two grid systems utilized are quite small.
(4) The data simulated in the present study almost coincide with Itoh's calculated results for an ATDC of less than 25°.

Acknowledgments

The authors are indebted to the National Science Council of the Republic of China for its financial support and assistance with this project (No. NSC79-0401-E006-19).

References

1 Shyy, W., Tong, S. S., and Correa, S. M. Numerical recirculating flow calculation using a body-fitted coordinate system. *Num. Heat Transfer*, 1985, **8**, 99–113
2 Shyy, W. A numerical study of annular dump diffuser flows. *Comput. Meth. Appl. Mech. Eng.*, 1985, **53**, 47–65
3 Pope, S. B. The calculation of turbulent recirculating flows in general orthogonal coordinates. *J. Comput. Phys.* 1978, **26**, 197–217
4 Anderson, D. A., Tannehill, J. C., and Pletcher, R. H. *Computational Fluid Mechanics and Heat Transfer*, Hemisphere, 1984, Chap. 10
5 Thompson, J. F., ed. *Numerical Grid Generation—Foundations and Applications*, North-Holland, New York, 1982
6 Chiu, C. P. and Wu, T. S. A numerical solution of the in-cylinder steady flow in nonorthogonal curvilinear coordinate system, Accepted for publication by *J. Chinese Inst. Engrs.*, 1990
7 Chiu, C. P. and Wu, T. S. Study of the flowfields of irregular shaped domain by an algebraic grid generation technique. *Int. J. ASME*, Series II, 1990, **33**(3) (in press)
8 Gosman, A. D. and Johns, R. J. R. Development of predictive tools for in-cylinder gas motion in engines. SAE 780315, 1978
9 Kondoh, T., Fukumoto, A., Ohsawa, K., and Ohkubo, Y. An assessment of a multi-dimensional numerical method to predict the flow in internal combustion engines. SAE 850500, 1985
10 Chiu, C. P., Wu, T. S., and Chou, H. M. Numerical simulation of in-cylinder air motion. *Proc. 3rd CSME Conf.*, 1986, 389–400
11 Chiu, C. P., Wu, T. S., and Chou, H. M. Numerical simulation of turbulent and laminar flow in internal combustion engines, *Proc. 4th CSME Conference*, 1987, 229–242

12 Shah, P. and Markatos, N. C. Computer simulation of turbulence in internal combustion engines. *Int. J. Num. Meth. Fluids*, 1987, **7**, 927–952

13 Itoh, T., Takagi, Y., Ishida, T., Ishikawa, S., and Ishikawa, T. Analysis of in-cylinder air motion with LDV measurement and multi-dimensional modeling. *Proc. Int. Symp. on Diagnostics and Modeling of Combustion in Reciprocating Engines*, Tokyo, Japan, September, 1985, 185–192

14 Chiu, C. P. and Wu, T. S. Study of air motion in reciprocating engine—using an algebraic grid generation technique. *Num. Heat Transfer*, Part A, 1990, **17** (in press)

15 Moretti, G. and Abbett, M. A time-dependent computational method for blunt body flows. *AIAA J.*, 1966, **4**(12), 2136–2141

16 Morel, T. and Mansour, N. N. Modeling of turbulence in internal combustion engines. SAE 820040, 1982

17 Ikegami, M., Kidoguchi, Y., and Nishiwaki, K. A multi-dimensional model prediction of heat transfer in non-fired engine. SAE 860467, 1986

18 Launder, B. E. and Spalding, D. B. *Lectures in Mathematical Models of Turbulence*, Academic Press, London, 1972, Chap. 5

19 Khalil, E. E. *Modeling of Furnaces and Combustors*, Abacus Press, Chap. 3, 1982

20 Patankar, S. V. *Numerical Heat Transfer and Fluid Flow*, McGraw-Hill, New York, 1980